Article:
Zhang, K., O Brádaigh, C. orcid.org/0000-0002-8048-4222 and Yang, D. (2026) High-performance curved sections in 3D printed continuous carbon fibre reinforced thermoplastic composites using aligned fibre deposition. Composites Science and Technology, 275. 111460. ISSN: 0266-3538

https://doi.org/10.1016/j.compscitech.2025.111460

Composites Science and Technology 275 (2026) 111460

Contents lists available at ScienceDirect

Composites Science and Technology

journal homepage: www.elsevier.com/locate/compscitech

High-performance curved sections in 3D printed continuous carbon fibre reinforced thermoplastic composites using aligned fibre deposition

Ka Zhang [a], Conchúr Ó Brádaigh [b], Dongmin Yang [a,*]

[a] School of Engineering, Institute for Materials and Processes, University of Edinburgh, Edinburgh, EH9 3FB, UK
[b] School of Mechanical, Aerospace and Civil Engineering, University of Sheffield, S10 2TN, Sheffield, UK

ARTICLE INFO

Keywords:
3D printing
Continuous carbon fibre reinforced thermoplastic
Fibre misalignment
Curved beam
Image-based modelling

ABSTRACT

This paper presents high-performance curved sections in 3D printed continuous carbon fibre reinforced thermoplastic composites using an aligned fibre deposition (AFD) method on a 6-axis robotic arm. 3D printed curved composite beams using both AFD and conventional methods are mechanically tested under four-point bending and scanned by X-ray computed microtomography (μCT) to characterise the fibre distribution and develop image-based finite element models. Compared to conventional printing method using a commercial nozzle, the proposed AFD method significantly improves the fibre alignment and reduces void content in the printed composites, and the curved beam strength is calculated as 204.2 N and 224.5 N for the cases of 7 mm and 15 mm radius of curvature, achieving an improvement of 34.0 % and 45.3 %, respectively. The modelling produces excellently matched stiffness with the experimental measurement, providing useful insights into the stress and strain distributions. The combination of experimental data and modelling results shows that the alignment of fibres in the curved composite beams plays a key role in improving mechanical performance and determining the final failure mode.

1. Introduction

Additive manufacturing (AM, also known as 3D printing) of continuous carbon fibre reinforced polymer composites has seen rapid development in the past decade, mainly due to its unique advantage of tailoring the fibre placement to form composites with complex shapes [1–3]. Material extrusion-based AM, such as fused filament fabrication (FFF), is commonly adopted for the 3D printing process of composites. Continuous carbon fibres (usually 1K or 3K fibre tow) are impregnated with a thermoplastic matrix either in-nozzle [4] or prior-printing [5]. The used nozzle [4,5] normally has a conical outlet to bypass the continuous fibres smoothly, as shown in Fig. 1a. Gantry systems [6] or multi-axis systems are normally used [7] to deposit the impregnated continuous fibres layer by layer. These printers have shown the capability to deposit continuous fibre composites along complex paths [6].

According to the study by Matsuzaki et al. [8], the smallest radius of curved sections that can be printed successfully using a 1K fibre bundle is 4 mm. However, the printed curved sections may have defects such as fibre breakage. Shiratori et al. [9,10] investigated the bending performances of the curved sections with inner radii of 2, 5, 10, 15 and 20 mm. They found the circumferential compression stress and circumferential elastic modulus decreased significantly for the radii of less than 10 mm and 5 mm, respectively. Although there is no recommended printing radius at present, the radii used in 3D printing are much smaller than the results achieved by other automatic manufacturing methods such as automated fibre placement (AFP). For example, a steering radius larger than 400 mm is recommended for a CF/PEEK tape with a width of 6 mm [11] because the fibre wrinkles occur in curved paths with smaller radii [12]. Therefore, the printing of small radii shows the potential for manufacturing complex parts with curved paths, such as optimised paths [13] and curved sliced parts [14].

Manufacturing defects, however, including fibre misalignment [15], fibre folding [8], air voids [16], fibre breakage [17], *etc.*, exist in the 3D-printed curved composite part. One of the major challenges is the disorder of individual fibres introduced by the printing process. Fibre misalignment, for example, based on our previous study [18], is primarily caused by the small bending radius (0.6 mm) at the outlet of the nozzle (see Fig. 1a). The maximum fibre misalignment angle is related to the diameter of the filament and the bending radius at the nozzle outlet, which can be expressed as the following formula [18]:

* Corresponding author.
E-mail address: Dongmin.Yang@ed.ac.uk (D. Yang).

https://doi.org/10.1016/j.compscitech.2025.111460
Received 14 February 2025; Received in revised form 22 August 2025; Accepted 24 November 2025
Available online 25 November 2025

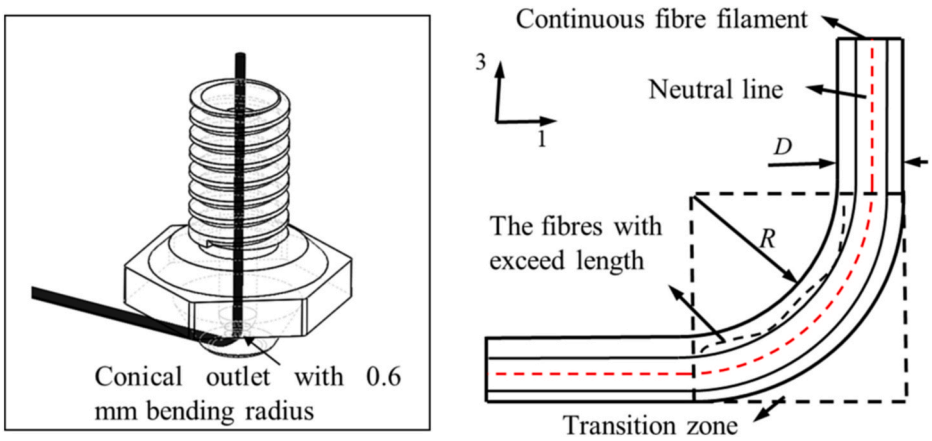

Fig. 1. (a) The schematic of the printing nozzle and (b) the continuous fibre filament at the outlet of the nozzle [18].

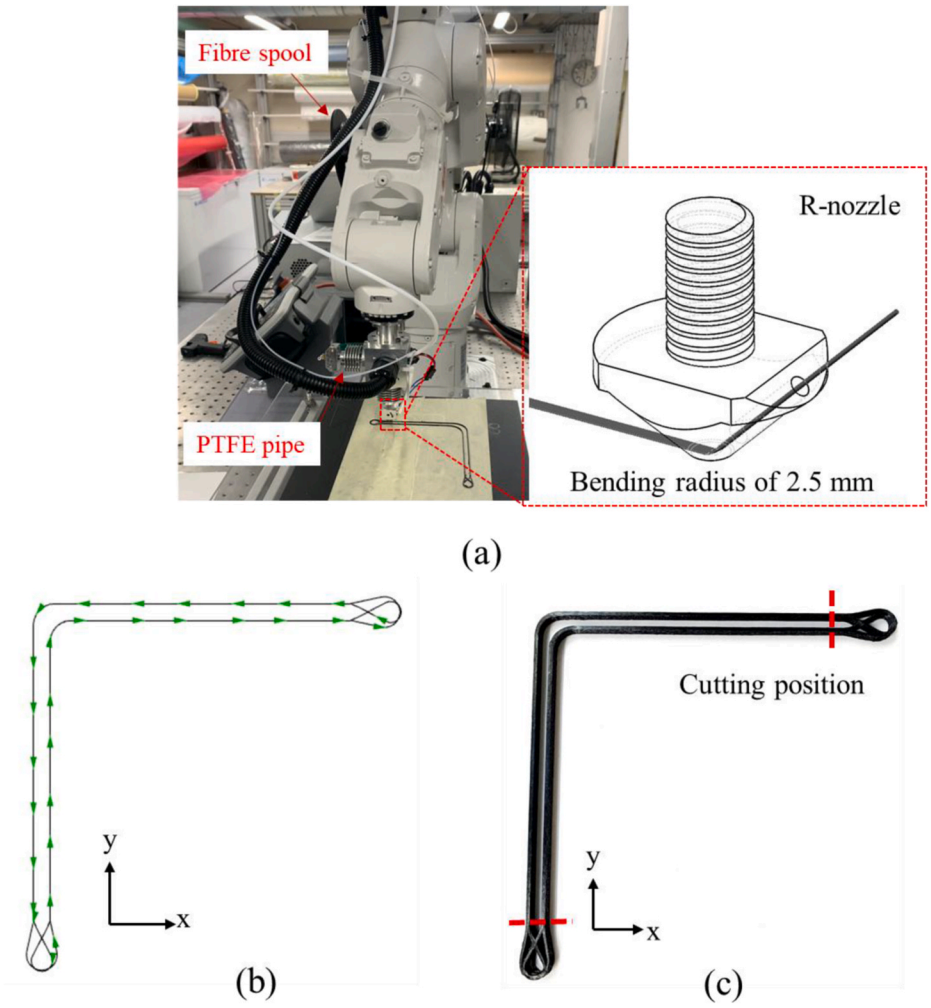

Fig. 2. (a) Robotic printing system, (b) top view of printing trajectory and (c) printed parts for curved beam samples.

$$\frac{D\pi}{4R} = \sqrt{1+\tan(\theta_{max})^2}\cdot E\left(\frac{\tan(\theta_{max})^2}{1+\tan(\theta_{max})^2}\right) - \frac{\pi}{2} \quad (1)$$

Where D and R are the diameter and inner bending radius of the filament elbow, respectively, as shown in Fig. 1b. $E(m)$ is the elliptic integral of the second kind and θ_{max} is the maximum misalignment angle.

Fibre folding, on another hand, occurs at the printed curved sections and is caused by the non-rotational movement of the nozzle [8,18], in which the filament is not driven to align with the curved path and would twist during printing [15,19]. Fibre folding would cause a nonuniform tow width, leading to stress concentrations in the folding area. As a side effect, air voids and fibre breakage are introduced into the printed part due to the excessive deformation of the filament [18]. As a result, the mechanical properties of 3D printed parts are weaker than those from traditional manufacturing with the same fibre content, such as AFP and

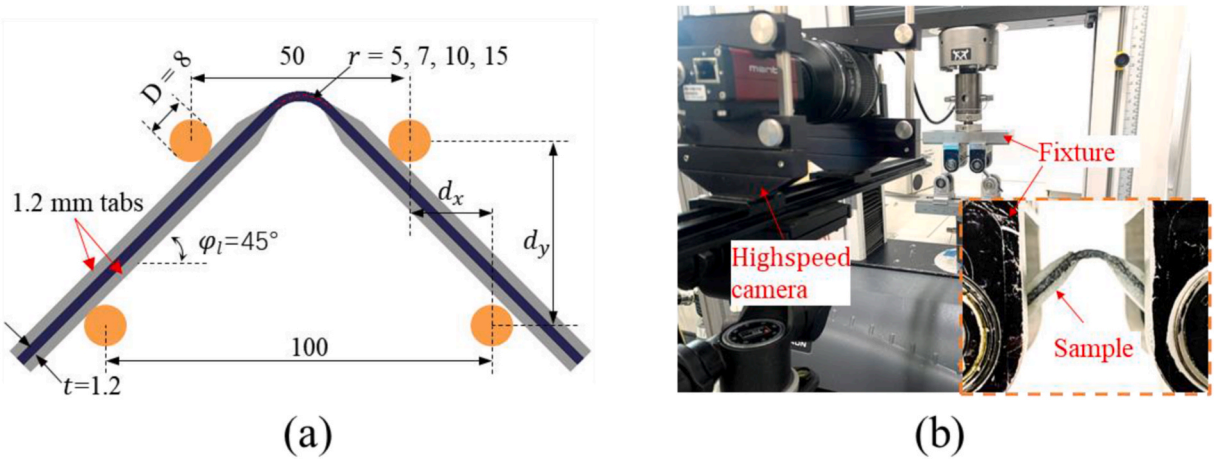

Fig. 3. (a) Schematic diagrams of samples for the curved beam test and (b) experimental configuration for the curved beam test.

compression moulding [20]. This eventually creates barriers to wider adoption of the 3D printing process in the composites industry.

To our best knowledge, very few studies have been devoted to specifically improving the fibre alignment during printing even though many devices such as lasers [9], microwaves [10], ultrasound [11] and compaction [7] are being used to integrate with the printing process for improving the printing performance. Based on the understanding of the deposition mechanism, we developed an aligned-fibre deposition (AFD) method with a customised nozzle [18], which is proven to be easily adapted in low-cost 3D printers and can substantially mitigate fibre misalignment during straight paths. The printed curved section, however, which is the most important part of composite printing, is not fully studied due to difficulties in characterisation and testing. The fibre orientation at the cross section is difficult to quantify using Yurgartis' method [21] because of the curve geometry. It would also be difficult to identify and establish the relationship between the mechanical performance and the printing defects without a sufficiently good knowledge of the microstructure of the curved section. To what extent the fibre orientation is improved by AFD and how this would impact the mechanical properties of the printed curved composite is still an important question to answer.

In this work, we report firstly the improved curved section using the new AFD printing method and study the curved section by tracing the individual fibre distribution based on X-ray computed microtomography (μCT) images and by developing image-based finite element models to aid with the experimental tests and characterisation. The paper is organised as follows: Section 2 describes the methodology for the AFD robotic printing system, the printing and testing experiments of specimens, the characterisation and image-based modelling. Section 3 presents the results and discussion. Application cases are presented in Section 4. The main conclusions are drawn in Section 5.

2. Methodology

2.1. AFD method and robotic printing system

The AFD method consists of a customised nozzle and a rotational printing system. The nozzle ('R-nozzle') is designed with an inclined passage hole at 45° and a large bending/deformation radius (2.5 mm) at the nozzle outlet, compared to the 0.6 mm bending radius of the commercial Markforged nozzle (M-nozzle), as shown in Fig. 2a. The purpose of the large radius is to overcome the excessive filament deformation based on Eq. (1). The outlet of the new designed nozzle is machined to a rectangular shape to provide more uniform pressure on the printed stripe, comparing to the conical shape in M-nozzle.

In this study, an ABB 6-axis robotic arm is used to drive the nozzle to deposit the fibre bundle along path-aligned directions, *i.e.*, the nozzle synchronously changes its laying direction in line with the tangential direction of the curved paths. It is worth noting that the robotic printing system is developed for fully extending the AFD method for this and future works, but for low-cost usage, a modified desktop 3D printer we reported before [18] can also achieve the results in this work. The nozzle associated with a hot end is mounted on the robot arm. The rotational axis of the nozzle is aligned with the 6th axis of the robotic arm to maximise the rotation range while avoiding the motion singularity of the arms, as shown in Fig. 2a. The rotation range of the nozzle is limited to ±360° to avoid the tangling of cables and filaments.

2.2. Sample preparation and mechanical testing

As previously mentioned, most of the currently developed printing methods for continuous carbon fibre reinforced polymer composites employ nozzle with vertical deposition channel with a conical outlet [22,23], similar to that of Markforged. To enable a direct comparison with the AFD method, a nozzle purchased from Markforged (M-nozzle) is used to represent the conventional printing method and its samples are used as control samples. It should be noted that the Markforged nozzle does not represent all manufacturing approaches, for example the methods using a needle-like nozzle [24] or a roller [25].

Curved-beam samples are used to value the mechanical performance of composite laminate with curved section, based on refs. [9,10]. Since the in-plane fibre misalignment is more dominant in the printed sample [15], it is reasonable to stack up the printed single-path stripe into multiple layers, similar to the printing method reported in Refs. [9,10], to exclude the unexpected influence of potential defects between multiple print paths, and mechanically test it to investigate how the fibre folding and fibre misalignment affect the mechanical performance of the printed composites as well as assess the effectiveness of the new nozzle (R-nozzle).

Curved-beam samples are printed and trimmed as shown in Fig. 2b and c. A total number of 100 layers are stacked and the layer thickness is set at 0.1 mm, following previous studies [15,18] to ensure stable adhesion to the print bed. The print trajectories, shown in Fig. 2b, are designed to continuously print the samples. The printing direction in each layer is set to be identical to minimise the manufacturing inaccuracy caused by layer stacking. When printing the samples with the M-nozzle, the same printing paths are used and only the rotational movement of the M-nozzle is deactivated. The printing path is converted into a series of polylines and its tangential direction is used to determine the nozzle coordinates and orientation. The path is converted to rapid code for the ABB robot arm. To minimise the system differences, only the nozzles are interchanged in the robotic printing system for the printing

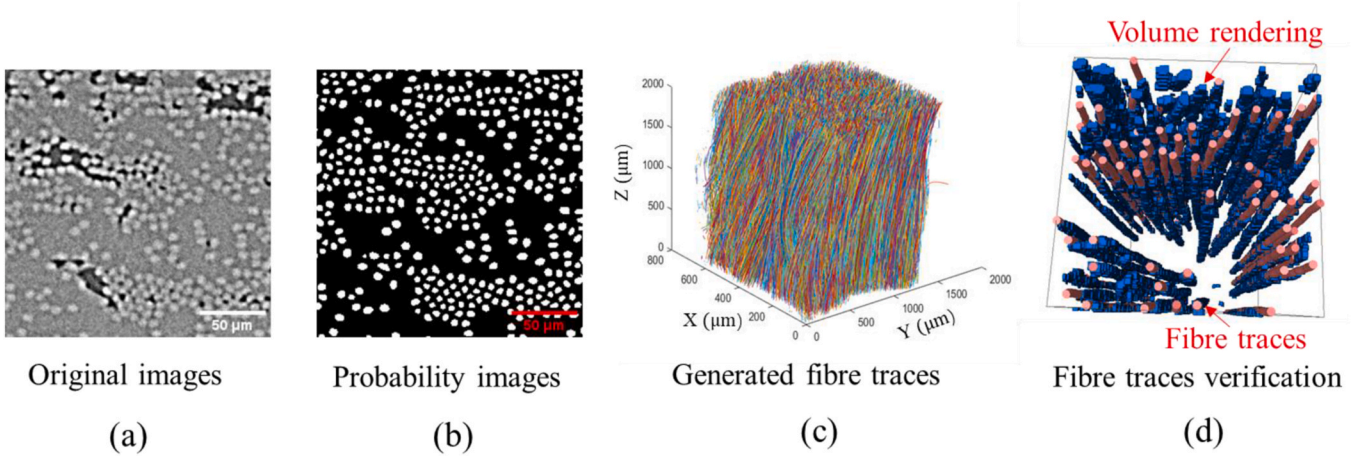

Fig. 4. μCT image processing flow (a) scanned images, (b) probability image processed by trainable Weka segmentation, (c) fibre tracing result and (d) fibre traces verified in Avizo.

of all the samples and the same printing parameters such as temperature, layer thickness, speed and trajectories are used to reduce variations between the two methods. Note that more details on the differences between two nozzles, which may affect the printing quality, such as stain/stress distribution, can be found in previous study [18].

The continuous carbon fibre reinforced thermoplastic filament used in this study is also purchased from Markforged. Since the material constituents are not disclosed by the manufacturer, its material constituents are investigated to be T300 carbon fibre and PA-6 (polyamide 6) matrix [26]. The composite filament has a diameter of 0.38 mm and a fibre volume fraction of 34 %. Like our previous work [15], a printer temperature of 245° is adopted. A maximum printing speed of 300 mm/min is used to ensure the printed stripe well adheres to the printer bed or substrate layers. A PTFE tube is inserted into both printer nozzles to guide the composite filament and prevent it from being overheated in the heating chamber. The feeding mechanism is deactivated and thus the composite filament is passively pulled out to adhere to the printer bed or substrate layers.

The printed parts are trimmed using a wet saw according to the ASTM test standards, *i.e.*, ASTM 6415 for the curved beam test. All the specimens are tabbed with a 1.2 mm thick glass fibre epoxy at both ends (see Fig. 3a). The tabs are sharpened to reduce stress concentrations at the grip section [9] and to ensure the load is appropriately passed through the tab onto the curved section. Eventually, the curved beam specimens have legs of 75 mm. The specimens have a width (w) of 10 ± 0.05 mm and a thickness (t) of 1.2 ± 0.1 mm. The configuration dimensions of the tests and samples are shown in Fig. 3b. Curved-beam parts with different radii, including 5.0 mm, 7.0 mm, 10.0 mm and 15.0 mm, are printed and tested to fully verify the mechanical behaviour of the printed curved section with different bending radii.

The curved beam test is carried out on an INSTRON 3369 machine with a 10 kN load cell, and a loading speed of 1 mm/min. The surfaces of samples are marked with fine speckle patterns and the test is recorded by a high-speed camera to obtain 2D full-field digital image correlation (DIC) results in the curved section. To distinguish the samples fabricated by the R-nozzle and the M-nozzle, the samples are labelled as R-case and M-case, respectively.

2.3. Characterisation

A μCT machine (ZEISS Xradia 620 Versa, Manchester, UK) and a scanning electron microscope (SEM, JSM IT-200) are used to observe the printed stripes. The μCT system provides high-resolution scans of the curved sections, which were used for the fibre tracing process. Curved sections with 5 plies/layers are prepared and the middle portions of the curved beam were trimmed to dimensions of 1.2 mm × 0.5 mm × 4 mm. These trimmed sections are placed on a wood stick for scanning. The scanning view is set to include the width and thickness of the curved section, allowing for an analysis the fibre distribution within a single tow. A voltage of 50 kV and a current of 90 A is set on the μCT scanner to achieve the optimum image quality with a voxel size of about 0.76 μm. The total exposure time for each scan is 18 h to obtain a wider intensity. The SEM is used to observe the fracture surface of the broken samples after testing. The samples are trimmed, mounted on a base, coated with a thin layer of gold to enhance conductivity before being examined in SEM.

The fibre tracking process is detailed as follows. First, the reconstructed images (Fig. 4a) are processed in ImageJ using trainable Weka segmentation [27], a machine training tool which can distinguish fibre, matrix and air voids by the labels and generate possibility images, as shown in Fig. 4b. Second, the possibility image is segmented by the threshold segmentation method to obtain a binary image of the cross-sections of fibres. The centre coordinates of the fibre are then calculated based on the geometry centre of the cross section. Third, the individual fibres are traced by connecting the centre points of each layer using a modified method which was originally proposed in Refs. [28,29] due to its efficiency and accuracy, as shown in Fig. 4c. The fibre tracing algorithm is compiled in MATLAB and the outputs are stored as Avizo Lineset format for virtualization, as shown in Fig. 4d.

The tracing results depend on the quality of the obtained centre coordinates of the cross section of fibres. However, the existence of air voids and close fibres will affect the identification of fibres, especially causing discontinuous traces. For the highly wavy fibres in our cases, the original algorithm [28] is modified by adding registers to store the discontinued fibre paths. The fibre tracing can continue if nearby fibres can be found in the next few layers (10 layers in our case). In the original algorithm, points in one layer search for matching points within a set radius (typically the physical fibre radius) in the next layer. If matching points are found, the paths are connected, forming a continuous fibre trace. However, points that do not find matches will continue to search throughout the entire algorithm process. In this study, the search for unmatched points is stopped after attempting 10 layers (7.6 μm). The modified algorithm is provided in the Appendix A. Even so, discontinuous fibres still occasionally exist in the traced results due to the quality of the images. Fortunately, it will not affect the distribution statistics of the fibres. As shown in Fig. 4d, the locations of fibre traces are consistent with the fibres obtained by image rendering, which proves the validity of fibre traces.

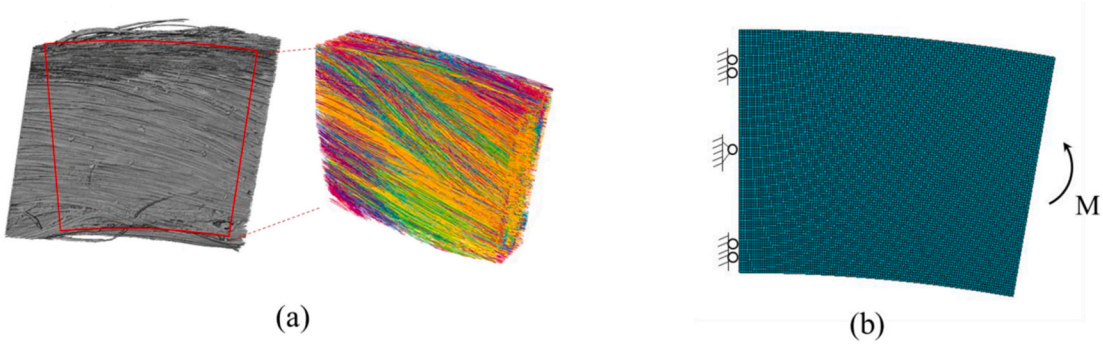

Fig. 5. (a) Schematic of the image-based modelling and (b) boundary conditions of the model.

Table 1
The material properties for T300 [41].

E_1 [GPa]	E_2 [GPa]	ν_{12}	ν_{23}	G_{12} [GPa]	G_{23} [GPa]
227	25	0.25	0.32	28	9.5

2.4. Image-based modelling

Considering the complex fibre distributions in this study, the finite element method (FEM) is employed to understand their behaviour in the curved sections, thereby enhancing the interpretation of the experimental results. Image-based models are constructed using the actual fibre distributions obtained in Section 2.3, enabling a more intuitive understanding of their impact on mechanical performance.

In a traditional model, the fibre and matrix are represented as separate bodies. The matrix often has a very complex geometry after Boolean operations, making it difficult and time-consuming to mesh. The commercial software Abaqus [30] provides an Embedded Element technology that allows the fibre and matrix to be modelled and meshed independently, offering an efficient alternative. In this method, fibres and the matrix are typically defined as embedded domains and host domains, respectively [31,32]. The fibres are enclosed within the matrix, and the translational degrees of freedom at their nodes are eliminated and calculated through interpolation of the nodes of the host [33]. The matrix-fibre interface is not defined by actual contact (e.g., cohesive zones or adhesive layers) but through node embedding constraints.

The Embedded Element method has been employed in numerous studies, such as those involving short fibre reinforced [31,32,34] and carbon nanotube reinforced composites [35]. Since the fibre and matrix are meshed separately, better mesh quality can be achieved, and the modelling and computational costs for complex models based on real images can be reduced.

Due to the limited projection area of the μCT images, only a small section of the curved beam could be scanned. However, the scanned region does cover the full width of a single tow, making it a suitable representation of fibre distribution along the curved section.

The fibre traces are imported into commercial CAD software (Rhino) as segments. Since uneven edges are observed on the width direction of printed parts, after translation and rotation, the fibre traces are cut by a box with the same radius of curvature as the printed section to remove the material caused by uneven edges. The cut traces are then converted into cubic splines with smooth operation and used to generate solid fibres with a diameter of 7.0 μm. The fibre geometries are imported into finite element software ABAQUS [30] for modelling.

Note that voids exist between the printed layers and would also affect the mechanical performance of the composite [36–38]. However, limited research specifically focuses on their influence in curved sections. Earlier studies [9,10] suggest that initial failure typically occurs at the outer compressed circumference of curved section, so investigations into the effects of voids and fibre misalignment on compression may provide insights. Previous study indicates that the initial fibre misalignment has a more pronounced effect than voids on performance [39,40], while the void shape and location can influence the compressive strength differently [37]. Chen et al. [40] reports that fibre waviness has a more significant effect on compressive failure than void content, with stiffness remaining largely unchanged and strength decreasing by less than 5 % as void content rises from 1 % to 5 %. Due to the complexity of the distribution and shape of voids in the 3D printed parts and the page limitation, the effect of the voids will not be discussed in this study. The matrix material is assumed to be fully resin-filled, with voids treated as resin-occupied.

The boundary conditions of the model are as shown in Fig. 5b, with a moment applied to the side face of the part. Since the analysis is limited to elastic behaviour, the same moment is applied to both cases to enable a comparative assessment of their stress and strain distributions. The matrix material used is PA6, with an elastic modulus of 2.7 GPa and a Poisson ratio of 0.2. The material properties used for the fibre (T300) are based on previous study [41] and shown in Table 1.

The model is constructed based on the actual microscopic fibre distributions, and its results are influenced by the selection of specimens and the regions of interest (ROI) chosen from the images. Therefore, it is necessary to verify the model's accuracy. Fibre distributions are affected by printing process parameters (such as temperature, pressure, and trajectory radius), and different choices of regions lead to different modelling inputs, which in turn affect the model outcomes. Given the limited image data and the high computational cost, this study analyses the accuracy and stability of the model by only selecting multiple ROIs within the 7 mm radius R-case.

Based on previous study, both the model size and the selected region influence the results. For the curved section, as the model must cover the entire radial region, its size is mainly determined by the thickness and the arc angle along the circumferential direction. In addition, the alignment between the extracted fibre box and the actual geometry also affects the fibre distribution in the model (see the alignment illustration in Table 2). Therefore, this study focuses on the effects of thickness, circumferential arc angle, and geometry alignment on the predicted results.

The modelling results (stiffness: $\Delta M_{uni}/\Delta\varphi$) are compared with the experimental average values to evaluate the accuracy of modelling. Meanwhile, the deviations and coefficient of variation (CV%) of the three factors (thickness, arc angle and geometry alignment) are analysed to assess the model's stability. The computed model results are presented in Table 2.

The results indicate that when the selected thickness is less than 0.2 mm (approximately two deposited layers), the model consistently underestimates the stiffness. The largest errors occur in models with either small circumferential arc angles (5°) or thin thicknesses (1 mm). A smaller circumferential angle truncates the fibres, probably making them more prone to rotation within the model and thereby reducing stiffness. Similarly, a thinner thickness exposes fibres at the lateral

Table 2
Sensitivity analysis of the image-based modelling.

Thickness	0.2 mm						0.1 mm	0.3 mm
Arc angle	5°			10°				
Alignment	0°			+2°	−2°	0°		
Location	1	2	3	Full capture				
Stiffness ($\Delta M_{uni}/\Delta\varphi$)	789.77	858.09	854.11	848.48	833.04	**847.22**	775.60	921.22
Accuracy (%)	−9.10 %	−1.24 %	−1.70 %	−2.35 %	−4.13 %	**−2.49 %**	−10.74 %	6.02 %
Deviation (CV%)	38.35 (4.60 %)			8.57 (1.02 %)			72.81 (10.68 %)	

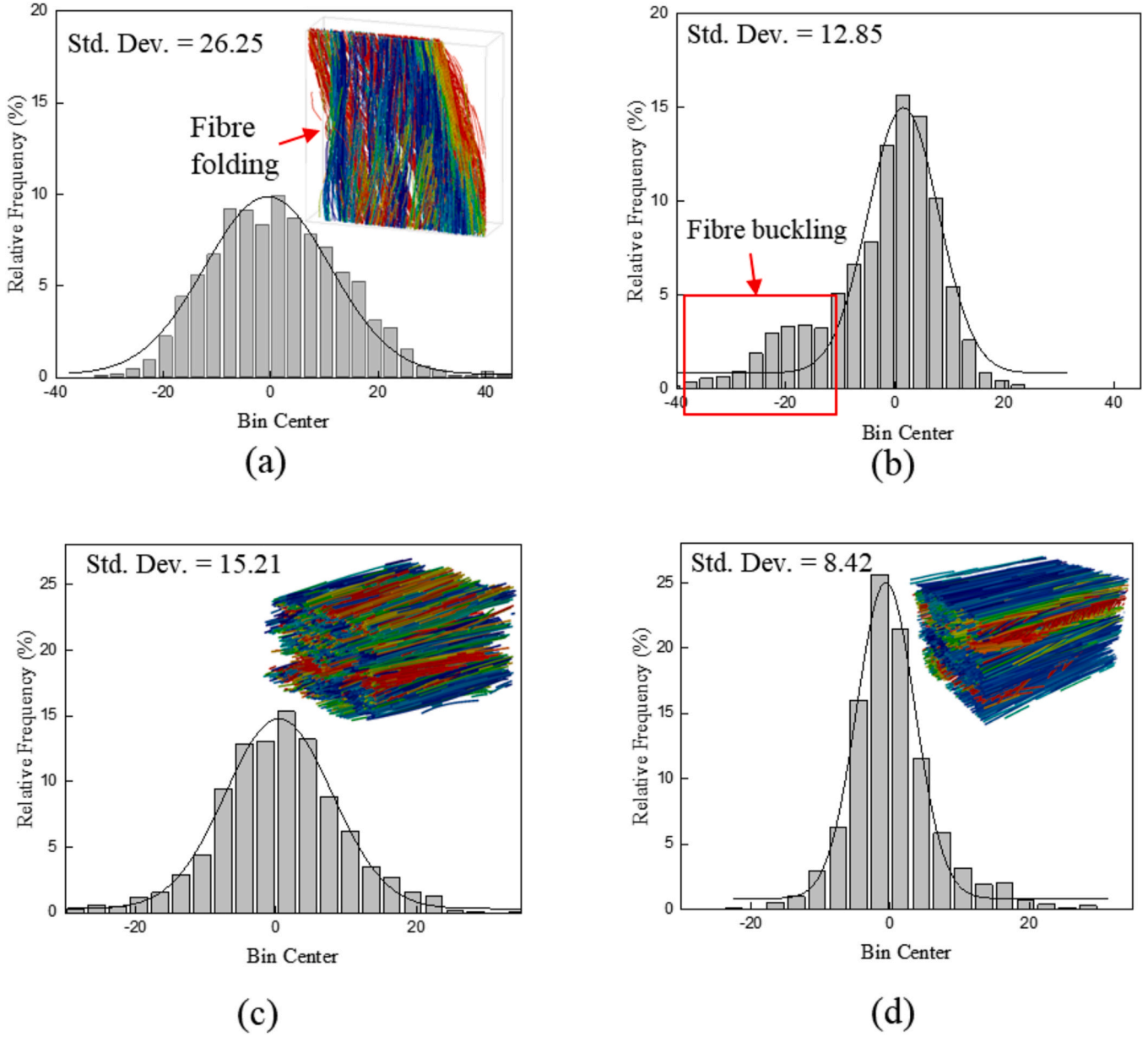

Fig. 6. Distribution of in-plane fibre misalignment angle for (a) M-case with radius of 7 mm and (b) R-case with radius of 7 mm, (c) M-case with radius of 15 mm and (d) R-case with radius of 15 mm.

surfaces, where outward rotation further decreases stiffness. When the thickness increases to 0.3 mm, the model slightly overestimates stiffness compared with experiments, but the deviation remains within an acceptable range (6.02 %). This discrepancy may be attributed to factors not accounted for in the model, such as voids.

The results also indicate that the model is insensitive to the

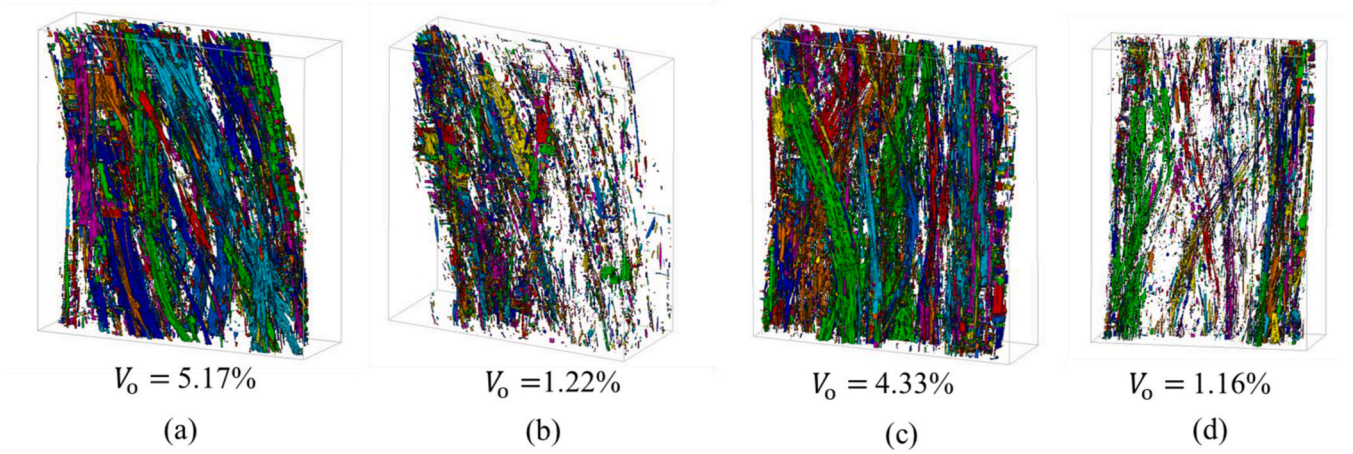

Fig. 7. Void distribution in (a) M-case with a radius of 7 mm and (b) R-case with a radius of 7 mm, (c) M-case with a radius of 15 mm and (d) R-case with a radius of 15 mm.

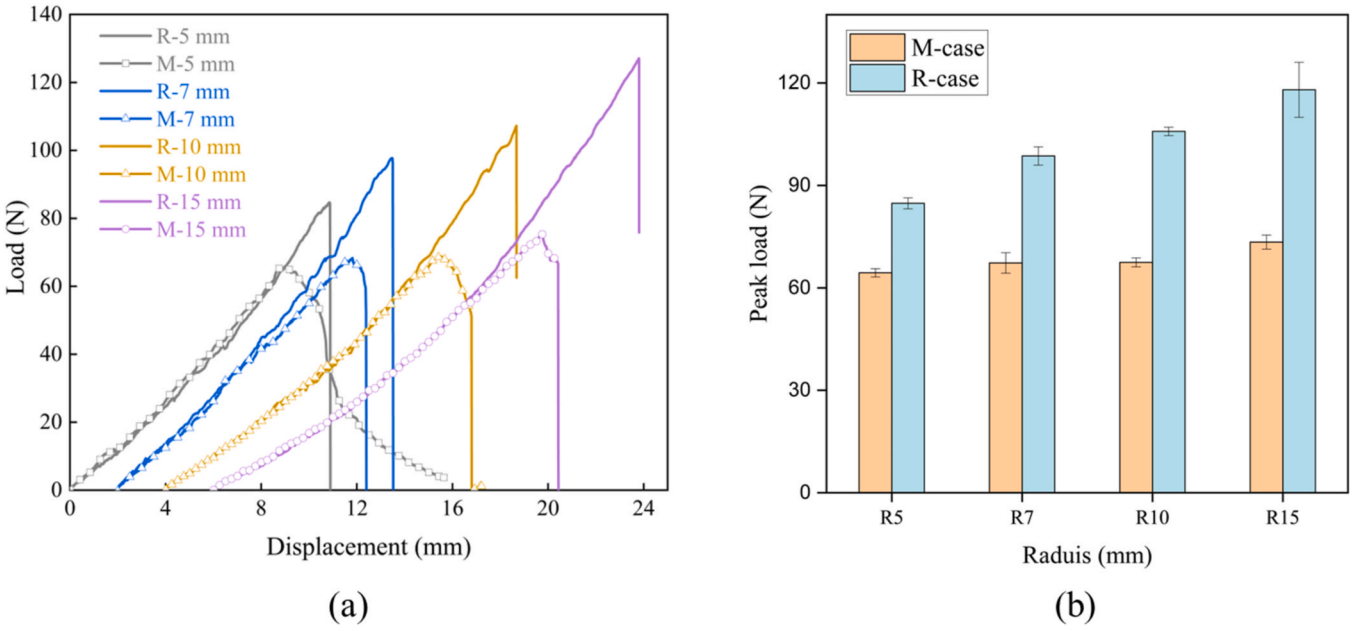

Fig. 8. (a) Load-displacement response of R-case and M-case with the radii of 5, 7, 10 and 15 mm and (b) the compare of the peak load of two cases. (Note that curves for different radii are offset in horizontal axis for better illustration).

alignment of the selected region. Rotating the region by ±2° produces negligible variation, likely because such small rotations introduce only in a global shift of fibre orientation with minimal effect on the internal fibre distribution. In contrast, the model is most sensitive to thickness selection, which leads to the largest deviations, while smaller circumferential arc angles also lead to prediction instability.

Overall, the best agreement with experimental data is achieved when using the maximum available circumferential angle (10°) and a thickness of 0.2 mm. Thus, the maximum circumferential angle and 0.2 mm thickness are adopted to modelling other cases, for high accuracy and less modelling costs (compared with the 0.3 mm case). It is worth noting that for the 7 mm radius curved section, the CT projection covers a maximum circumferential angle of 10°, while for the 15 mm radius case, the same projection area captures only 5°.

3. Results and discussion

3.1. Fibre misalignment and void distribution

During deposition, continuous fibre filaments undergo bending, compression, in-plane stretching, and bonding with the substrate. Excessive in-plane deformation, combined with uneven stress distribution, exacerbates fibre misalignment [18]. Here, the curved sections are aligned in-plane to investigate mechanical performance and highlight the R-nozzle's advantages, making in-plane misalignment particularly critical. The statistics of in-plane misalignment angle distribution for both cases are shown in Fig. 6. Meanwhile, the statistical results for out-of-plane fibre misalignment have been provided in the Appendix B to facilitate a more comprehensive understanding of the findings.

The angle between the fibre tangent and the tangent of the curved section is used to present the in-plane fibre misalignment angle in a curved section. The angle can be obtained in CAD software by interacting the fibre with a plane passing through the centre of the curved

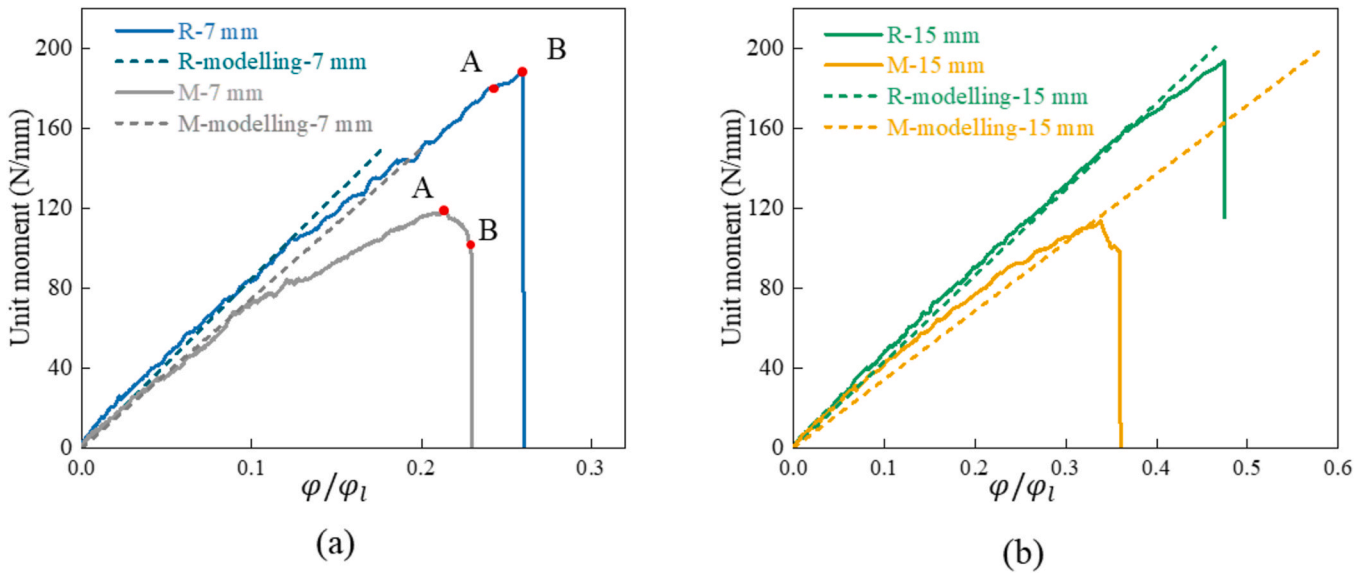

Fig. 9. Unit moment and normalised angular response of curved beam samples with curvature of radius of (a) 7 mm and (b) 15 mm.

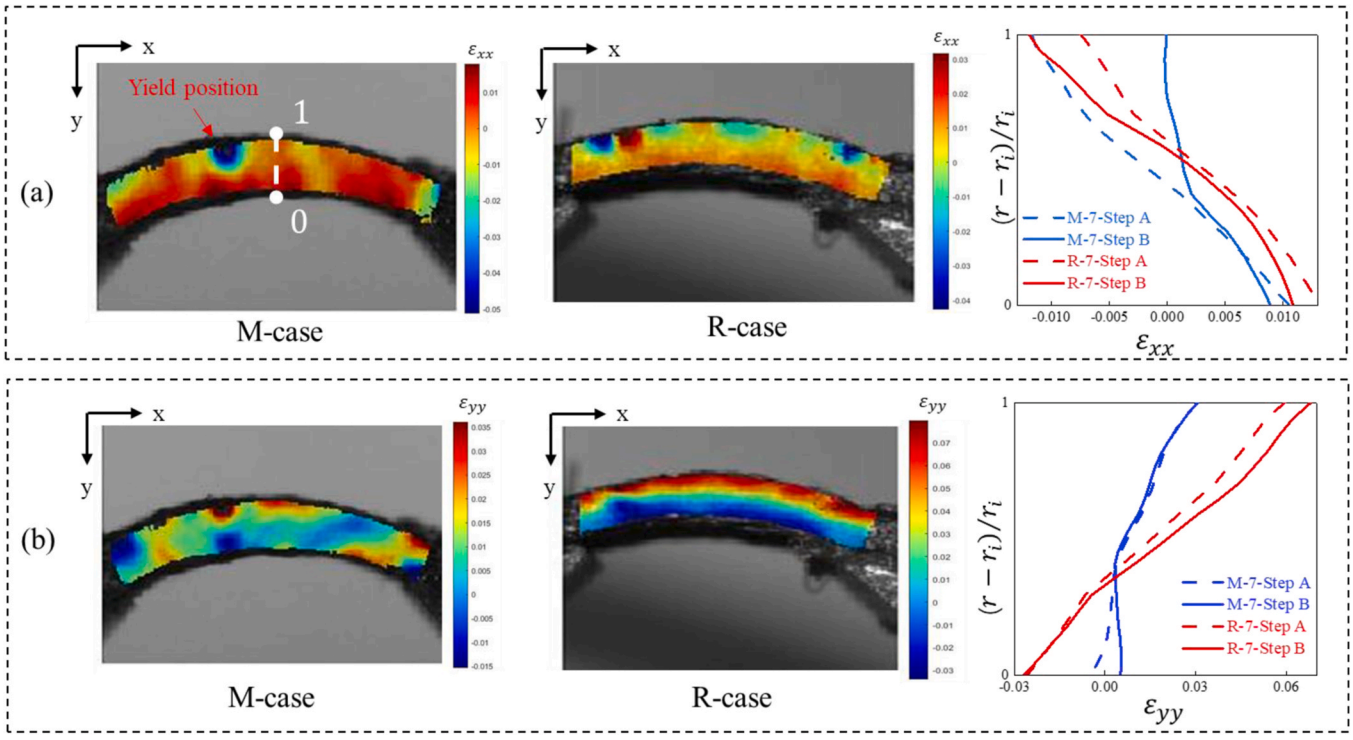

Fig. 10. Comparison of strain contours in the curved beam before failure: (a) ε_{xx} and (b) ε_{yy} from DIC.

section and calculating the angle between the fibre tangent and normal vectors of the plane. The distribution of fibre angles can be fit with a normal distribution (Gaussian distribution):

$$f(\theta) = \frac{1}{\sqrt{2\pi}\sigma_0} \exp\left(-\frac{(\theta-\mu_0)^2}{2\sigma_0^2}\right) \quad (2)$$

Where μ_0 and σ_0 are the mean and standard deviation (Std. Dev.), respectively.

Fig. 6a and b shows the in-plane fibre misalignment angle distribution in the cases of 7 mm radius curvature for both printing methods, with both mean angles near 0°. The R-case exhibits a smaller standard deviation (12.85) compared to the M-case (26.25), indicating better fibre alignment along the curved path in the R-case. The fibre misalignment in the R-case is not symmetrically distributed around the mean; instead, the more misaligned fibres fall between −40° and −10°. This is likely due to the buckling of some fibres on the inner radius of curved section, occurring at the bottom of the placed fibre bundle [18]. In contrast, the M-case exhibits a more even distribution on both sides of the mean, likely due to a consistent fibre folding pattern introduced during printing.

For the cases with a curvature radius of 15 mm, the standard deviations of both cases are decrease compared to those with a 7 mm radius, indicating improved fibre alignment at a larger print radius. The maximum fibre angles of both cases are around ±20°. The fibre angles of

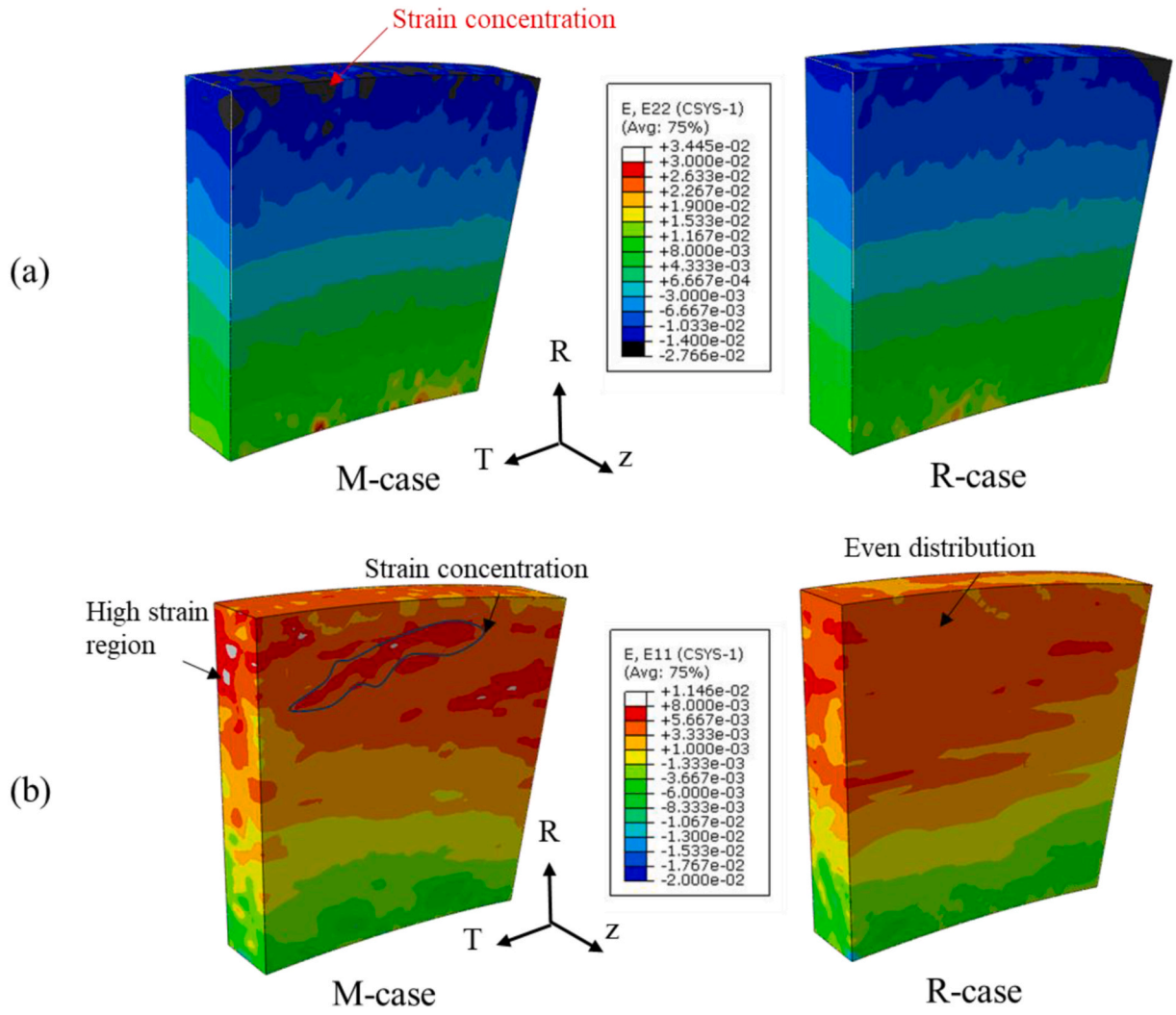

Fig. 11. Comparison of strain contours in curved beam before failure: (a) circumference strain and (b) radial strain from image-based modelling.

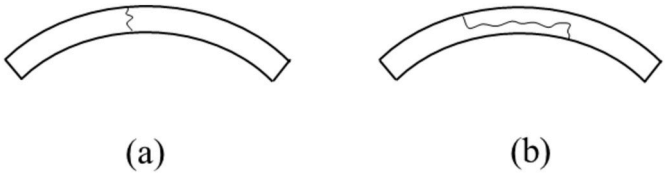

Fig. 12. The failure mode for (a) M-cases and (b) R-cases.

the R-case are more concentrated around the mean value, however, showing that more fibres are concentrated in the tangential direction of the curved beam and resulting in approximately half the standard deviations of the M-case (8.42 Vs. 15.21). The fibre distributions captured from the region of interest of the fibre traces are also shown in Fig. 6c and d. The colour of the traces represents the angle relative to the mean direction, with blue indicating smaller angles and red representing larger angles. In the M-case, fibre colours show an evenly dispersed distribution. In contrast, the R-case shows a clustered distribution of blue fibres, while red fibres, likely due to fibre buckling, appear in the interlayer regions. Therefore, it is proved the AFD printing method can improve fibre alignment in curved sections but there is still room for improvement, for example, the buckling fibres.

The void fraction of the curved section was quantified using Avizo software. Specifically, 2D tomographic images were first processed via threshold segmentation to identify void regions, which were then reconstructed into a 3D volume to obtain the total void volume. The void fraction is defined as the ratio of the void volume to the total material volume. Compared to traditional approaches based on 2D metallographic images, approximately 2000 images are analysed per case, providing more reliable results.

Fig. 7 shows the air voids in the curved section which are reconstructed in Avizo. With the AFD method, the void volume fraction (V_o) in the printed curved section with a 7.0 mm radius is reduced from 5.17 % to 1.22 %. In the R-case, more voids are concentrated on the inner side of the curved beam, aligning with the location where fibre buckling occurs. In contrast, the M-case shows an even distribution of voids throughout the area. The void distributions for both printing methods are mostly aligned with the printing direction, suggesting that the voids are primarily introduced during the printing process, likely as a by-product of excessive fibre movement [18]. The R-case with a 15.0 mm radius has a similar V_o compared with the 7.0 mm case and is significantly smaller than that of M-case (1.16 % vs 4.33 %). On the other hand, the tomographic images for of 7 mm radius cases and the metallographic images for its leg region is displayed in Appendix C to enhance understanding of the layer bonding and voids distribution. It is worth to mention that the void content is characterised to enable a detailed comparison of the microstructural differences between the two cases, providing a more comprehensive understanding of the factors that may influence the material's mechanical properties. However, as noted earlier, the effect

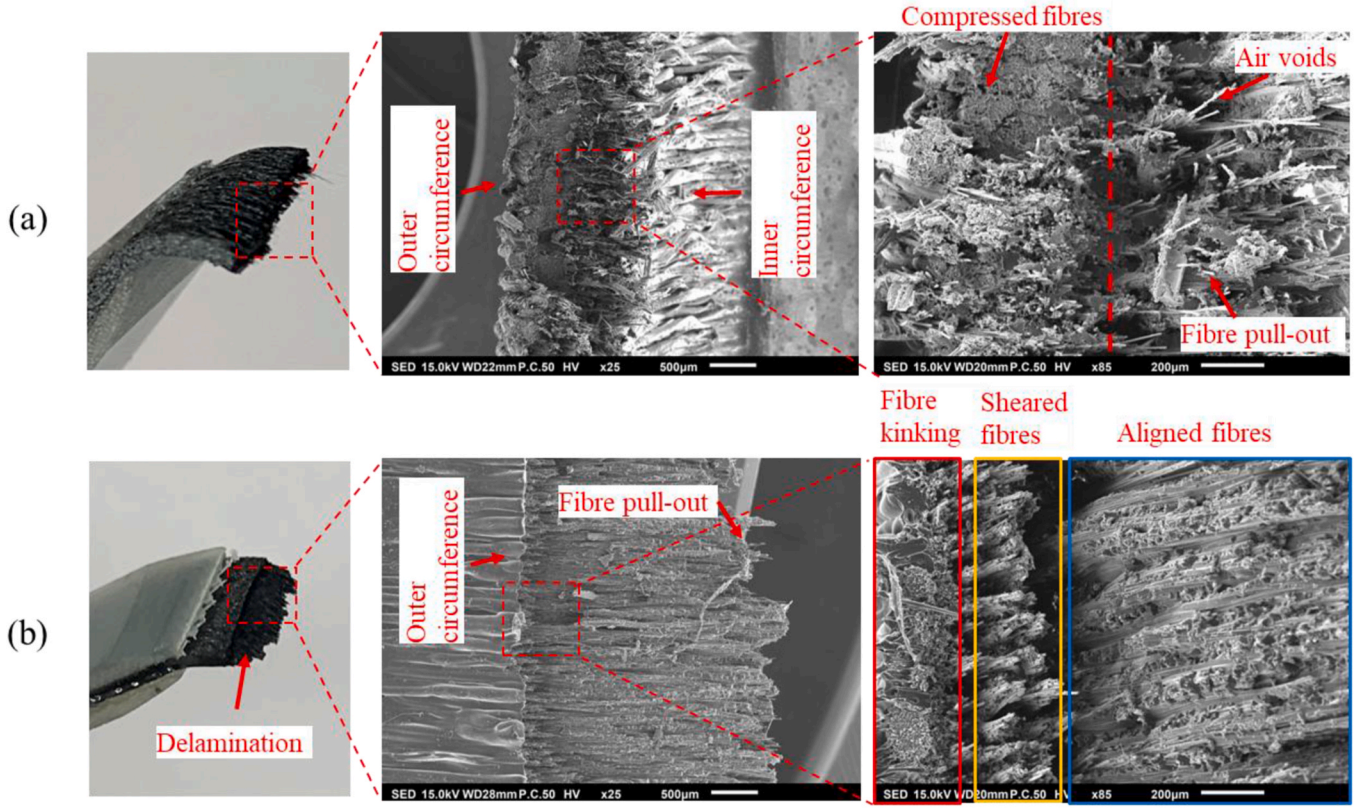

Fig. 13. SEM micrographs of the fracture surface: (a) M-case and (b) R-case with a radius of 7 mm.

of voids is not discussed in this study due to the complexity of voids distribution and shape.

3.2. Mechanical performance

Three specimens have been tested for each case. The load-displacement curves of the curved-beam test are shown in Fig. 8a, and the statistics of the peak loads for each case are presented in Fig. 8b.

As shown in Fig. 8a, the loading curves for specimens with the same curvature radius are nearly identical at the test's initial stage, probably because tabs were attached to both sides of the specimens, mitigating the effects of fibre misalignment on the stiffness of beam legs. The R-cases specimens fracture abruptly upon reaching peak load, while the M-cases show fluctuating load curves and a progressive, ductile failure after the peak load, likely due to the presence of highly waved fibres.

As shown in Fig. 8b, the peak load increases with the curvature radius of the beam for both printing methods. The R-cases consistently exhibit higher peak loads than the M-cases at each radius, showing an overall enhancement in strength. The maximum increase of 68.0 % (126.5 N vs. 75.3 N) can be seen in the 15 mm radius case. The standard deviations of the peak loads are relatively small, indicating consistent results. However, the R-case with a 15 mm radius exhibits the highest standard deviation. Observations show that the specimens tend to slip and lose alignment near the end of the test, which may be due to the larger radius of curved section, causing greater variability in the recorded results.

Since the part is subjected to pure bending moment during deformation, the moment can be obtained using by the following expression [42]:

$$M = \left(\frac{P}{2\cos(\varphi)}\right)\left(\frac{d_x}{\cos(\varphi)} + (D+t)\tan(\varphi)\right) \tag{3}$$

Due to the tabs attached, the legs of the curved beam are only slightly deformed during the test. Therefore, the angle of the loading arm φ can be calculated by Ref. [43]:

$$\varphi = \sin^{-1}\left(\frac{-d_x(D+t) + d_y\sqrt{d_x^2 + d_y^2 - D^2 - 2Dt - t^2}}{d_x^2 + d_y^2}\right) \tag{4}$$

Where P is the total force, d_x is the horizontal distance between the centre lines of two top and bottom adjacent rollers, as shown in Fig. 3a, D is the diameter of the cylindrical loading bars, and t is the specimen thickness, d_y is the vertical distances between two adjacent top and bottom loading bars [43]. The moment per unit width M/w at the first force drop of P which is also known as curved beam strength (CBS) can be calculated by:

$$CBS = \frac{M_{\max}}{w} \tag{5}$$

The average CBS for the R-case is calculated as 204.2 N for a 7 mm radius and 224.5 N for a 15 mm radius, while the M-cases show values of 152.4 N and 154.5 N for these respective radii. This represents an improvement of 34.0 % and 45.3 % for the R-case over the M-case. The enhanced performance of the 15 mm case is likely due to improved fibre alignment compared to the other cases.

Fig. 9 shows the bending deformation and moment response curves of the curved section. The vertical axis is the normalised moment (per unit width and thickness) and the horizontal axis is the bending deformation in normalised angle φ/φ_l, where, $\varphi_l = 45°$ is also half of the arc angle of the curved section in degrees which also equals the angle from horizontal of the specimen legs at the start of the test (see Fig. 3a). In all cases, the experimental curves are nearly linear until the later stage of testing. The R-case specimen shows a slightly larger stiffness than the M-case.

As shown in Fig. 9, the model produces a linear prediction curve, as fibre-matrix interfacial and material failure are not considered. For the

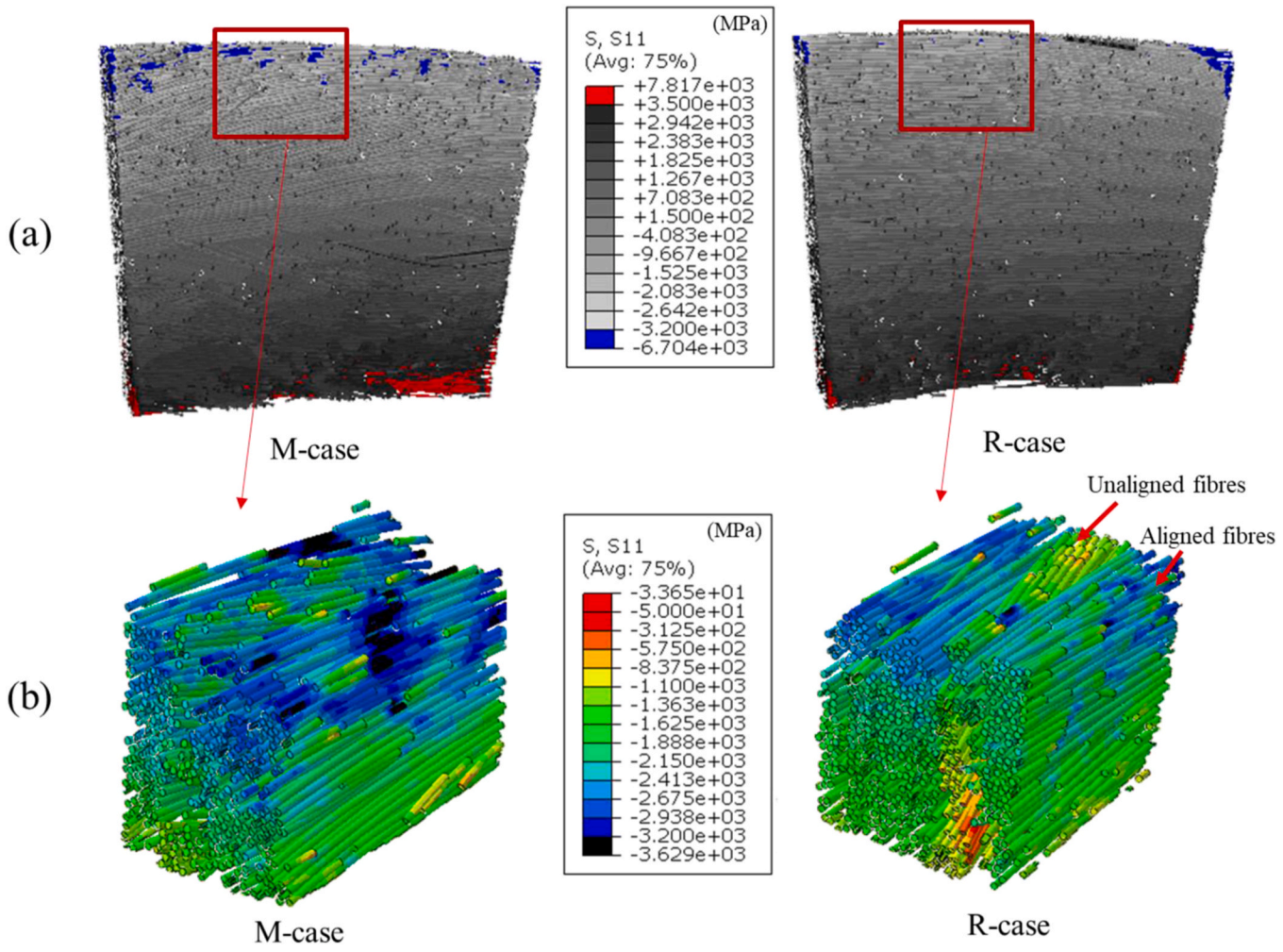

Fig. 14. Longitudinal stress of fibres (S11) in the curved beam of both cases with a curvature radius of 7 mm: (a) overall views and (b) zoomed-in regions.

7 mm radius case, the predicted bending stiffness agrees well with the experimental results, although it is slightly lower. According to the analysis in Section 2.4, this discrepancy is related to the size of the modelling. For the 15 mm radius cases, the predicted stiffness remains below the experimental values, with errors noticeably higher than those of the 7 mm radius case. The M-case exhibits the largest prediction error (−11.49 %), likely because the captured image covers only a limited arc angle, and a larger volume would be required to achieve more accurate predictions.

In summary, the model shows a reasonable agreement with the experimental results, demonstrating its validity. Therefore, it can be used to provide insights on the stress/strain distributions and failure modes of different cases in the following sections.

3.3. Strain distribution

Fig. 10 show the strain distributions of the curved sections with a radius of 7 mm, obtained experimentally from DIC. Due to the large bending deformation in the curved sections, the bending radius of the beam increases significantly during testing, making it challenging to convert the DIC data of the cured beams into polar coordinates. In this study, the strains in the *x*- and *y*-direction are used to approximate the circumferential and radial strains respectively, as the curved section is nearly flattened before failure. Specifically, ε_{xx} is the strain perpendicular to the load direction and ε_{yy} is the strain in the load direction. The strain results in the direction perpendicular to the load (ε_{xx}) are compared in Fig. 10a. The M-case demonstrates a significant strain concentration in the central region of the curved section prior to failure, where compressive yielding takes place. In contrast, the R-case shows both positive and negative strains on the left periphery, likely indicating out-of-plane buckling in the x-direction, which ultimately triggers material fracture. When the stress distribution along the midline (0–1) is analysed, the strain values reveal notable differences between the two cases. In the M-case, the strain on the outer circumference changes significantly before failure (from Step A to Step B, as marked in the test curve in Fig. 9a), with the absolute strain value decreasing to zero, indicating a stress release, likely due to material yield at the strain concentration site. In contrast, in the R-case, the absolute strain value on the outer circumference continues to increase until failure, leading to a sudden failure of the material.

The strain distribution in the load direction (ε_{yy}) of both cases are displayed in Fig. 10b. M-case shows multiple strain concentrations along both the inner and outer periphery of the curved section, while the R-case exhibits a uniform ε_{yy} distribution, with a distinct boundary between the inner and outer circumference, indicating a uniform deformation of the R-case sample. Compared with the results in Fig. 10a, the maximum strain value in the y direction (approximately radial direction) is greater than the strain in the x direction (approximately circumferential direction), probably because the fibres are mainly distributed along the circumferential direction, leading weak reinforcement in radial direction. When the strain values on the midline 0–1 is probed, the strain of M-case are approaching zero at the inner circumference ($(r-r_i)/r_i$ <0.4), as shown in Fig. 10b, probably relating to the fibre misalignment on the inner circumference of M-case, as

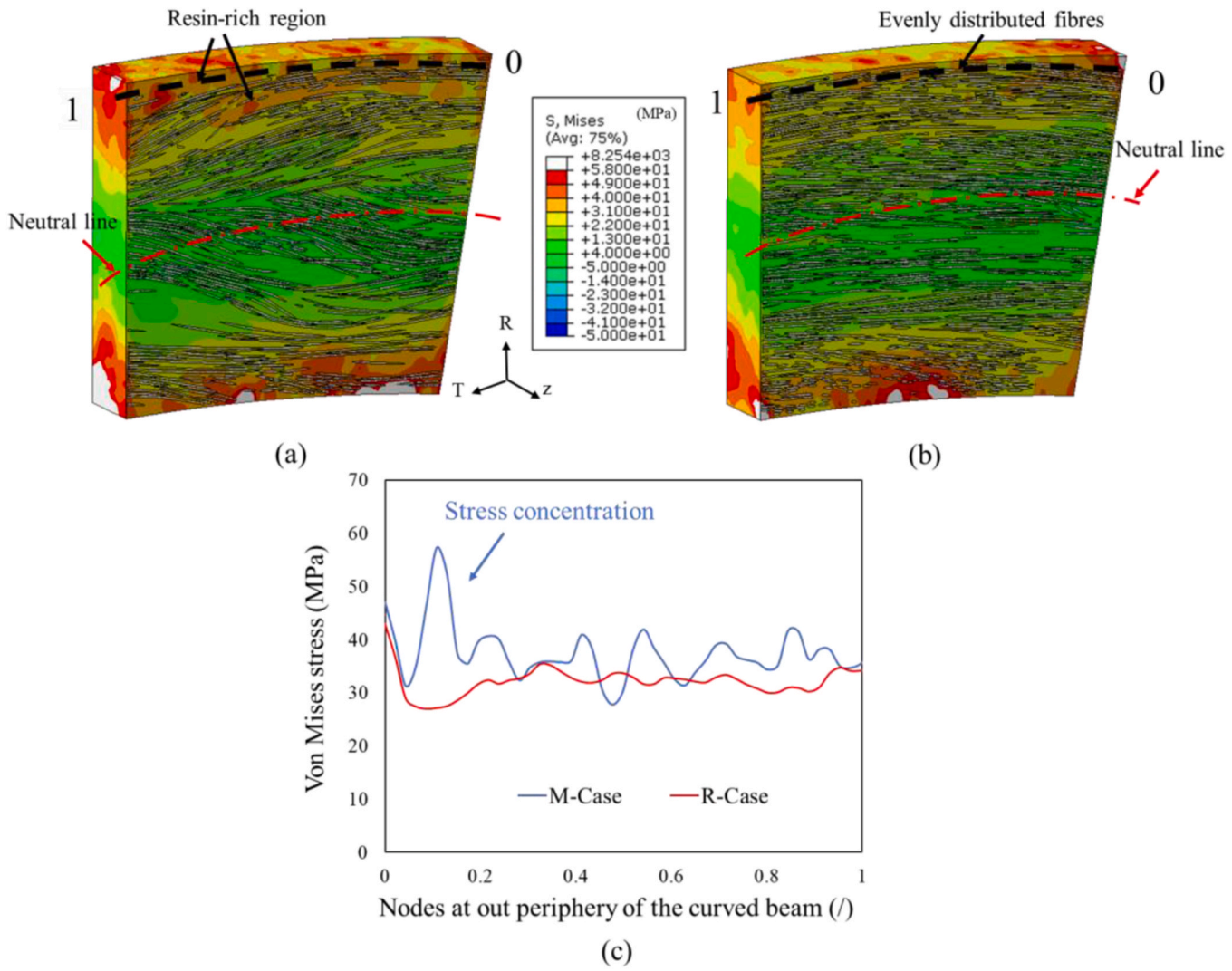

Fig. 15. Von Mises stress distribution in curved beam with a curvature radius of 7 mm: (a) M-case and (b) R-case; (c) von Mises stress value at the outer periphery (picked along a curve from point 0 to point 1).

shown in Fig. 6a. On the contrary, the strain distribution of R-case is approximately linear, which may benefit from the uniform fibre distribution.

The strain distribution calculated by the image-based modelling is converted into polar coordinates and shown in Fig. 11 to explain the experiment. For the circumference strain of the matrix, as shown in Fig. 11a, the M-case exhibits strain concentrations at the outside the circumference compared to the R-case, which is consistent with the DIC result and prone to causing yield of material and then leading to failure. The radial strain of M-case also exhibits strain concentrations (Fig. 11b), which are distributed along the circumferential direction, aligning with the orientation of the fibre bundles and coinciding with resin-rich regions. The strain concentration is likely caused by the non-uniform fibre distribution.

3.4. Failure modes

The samples printed with each method show the same failure mode for all the radii of curvatures. The M-cases yield at the middle of the curved section while the R-cases break with a split in the middle of the tow, as schematically shown in Fig. 12.

The SEM images of the fracture surface strongly support the different failure modes of the two cases. Taking samples of 7.0 mm radius as example, the fracture surfaces in the M-case are much rougher than the R-case, as shown in Fig. 13a. There is a distinct compressive fracture of fibres at the outer periphery, while the inner periphery shows clear fibre pull-out due to the progressive debonding of fibre-matrix interfaces, which is consistent with the observation in Refs. [9,10]. For the R-case (Fig. 13b), the failure area is divided into three regions. The outer side of the circumference shows neat fibre kinking due to compression, whereas the inner side of the circumference shows tensile failure. Fibres in the middle are sheared with rough fractures, probably because of the opposite circumferential stress directions on the inner and outer circumferences during failure.

The differing failure modes may be attributed to the fibre distribution in the two cases. As observed in the SEM images, the fibres in the R-case are noticeably more aligned compared to those in the M-case, consistent with the CT characterization results shown in Fig. 6. When the curved section is subjected to bending, the material on the outer periphery is under compression. The failure starts at the outer circumference because the compression strength of the composite is lower than the tensile strength [9,10]. The compressive strength may be influenced by the initial angle between the fibres [44], defined as the angle between the fibre's tangent and the tangent direction of the curved section in this study. Fibers with larger initial angles are more susceptible to buckling under compression, which explains the failure observed in the M-case. Conversely, when fibres are aligned with the curved section, the samples exhibit higher compressive strength but are more prone to delamination

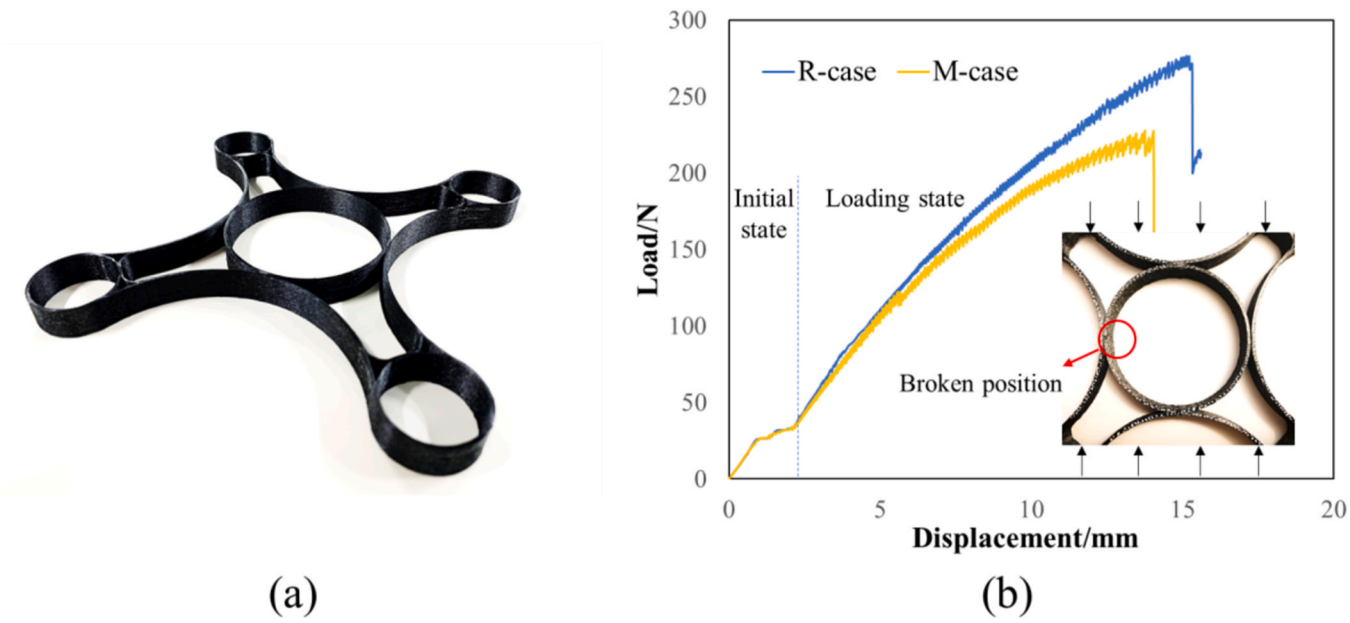

Fig. 16. (a) The demonstrator of a printed frame using the AFD method and (b) the compression response of the frames with R-case and M-case.

in the radial direction due to the absence of reinforcement, which explains the observed failure mode in the R-case. It is worth noting that the resin rich region and air voids that remain in the sample would also affect the failure mode. The voids may cause local buckling of the fibres and weak fibre-matrix bonding, which explains the uneven buckling surfaces and fibre pullout of M-case (as indicated in Fig. 13a), as well as the lower load-carrying capacity.

The model can explain the detailed stress distribution of the fibres. Fig. 14 illustrates the longitudinal stress of individual fibres in the two cases, with direction-1 representing the longitudinal direction of fibres. High-stress regions are located along the outer circumference of the curved section. As shown in Fig. 14a, the M-case exhibits more areas of stress concentration compared to the R-case, even under the same applied load. This explains the earlier failure observed in the M-case. Fig. 14b presents the zoomed-in views of the outer circumference, where high-stress regions are concentrated along the outer periphery and boundary areas. The R-case, with its relatively uniform fibre distribution at the boundaries, exhibits lower compressive stress on the fibres compared to the M-case. Furthermore, fibres aligned with the curved section experience higher stress compared to unaligned fibres, as they bear more of the compressive load along the curve. This suggests that higher strength can be achieved with better-aligned fibres.

As shown in Fig. 15, the von Mises stress distribution of the matrix (shown alongside the real fibres), reveals notable differences between the two cases. Since the curved section is subjected to bending, regions near the neutral line experience lower stress compared to the outer and inner peripheries. Both cases exhibit similar stress distributions near the neutral line, despite differences in fibre misalignment. However, significant differences in stress distribution are observed at the outer and inner peripheries due to varying fibre distributions.

Both fibre alignment and fibre distribution play crucial roles in influencing the material's stress distribution. In the M-case (Fig. 15a), high-stress regions are observed along the misaligned fibres on the outer circumference. Additionally, stress concentrations are primarily associated with resin-rich areas, which sourced from the uneven fibre distribution created by printing. In contrast, the R-case features a more aligned and uniform fibre distribution on the outer circumference, leading to lower and more uniform stress regions, as shown in Fig. 15b. When analysing the stress distribution along a curve (represented by black-dotted lines and positioned 12 μm away from the outer periphery of the curved section to reduce edge effects), the M-case shows a higher average stress value and more significant stress fluctuations compared to the R-case, as depicted in Fig. 15c. The stress concentration observed in the M-case explain the rough fracture surface following failure (as shown in Fig. 13a), whereas the uniform stress distribution within the material of R-case could attribute to the neat fracture surface.

4. Demonstrators printed by AFD

A composite frame is printed using the AFD to further illustrate its potential applications. The frame is shown in Fig. 16a, which is designed with circular arcs with smooth connection. The frame is printed with one single fibre path, which contributes to its lightweight structure. It has a height of 10 mm, a length and width of 120 mm, and an ultralight weight of 11.78 g. The continuous fibres are deposited aligning with the curve paths through the AFD robotic printing as can be seen in the attached video in Appendix D.

The frames printed using the AFD and Markforged nozzles are all tested under compression and the load-displacement response curves are shown in Fig. 16b. The frames show a large deformation in the loading direction, which reaches around 15 mm. Noting that both frames slip in the transverse direction (perpendicular to the load direction), and this leads to jagged load-displacement curves. At the beginning of the test, the curves of the two cases were identical, possibly because they share a similar structure and the deformation is small. When the load exceeds 30 N, the difference becomes clear. The R-case shows higher stiffness than the M-case and reaches a higher peak load as well, which proves the excellent performance of the AFD printed complex structure.

5. Conclusions

In summary, an aligned fibre deposition (AFD) method with a customised nozzle mounted on a 6-axis robotic arm is presented to reduce the printing defects and improve flexural properties of 3D printed curved beams using continuous carbon fibre reinforced PA-6 thermoplastic composites. The main conclusions drawn are as following:

(1) The AFD method reduces the standard deviation of the fibre misalignment angle distribution from 15.21 to 8.42 and the air void content from 5.17 % to 1.22 % on the curved section with radius of 15 mm, as compared to the conventional printing method.

(2) The AFD method achieved a curved bending strength of 204.2 N and 224.5 N for the radius of 7 mm and 15 mm respectively, with improvements of 34.0 % and 45.3 % over the conventional method.
(3) The DIC experimental measurements and image-based finite element modelling show strong correlation, both confirming the observed failure modes. In the R-case, fibre kinking occurs on the outer circumference of the curved section, accompanied by delamination along the middle plane. In contrast, the M-case exhibits plastic yielding at the midsection of the beam. These results highlight the significant influence of fibre alignment and distribution on the overall strength of the samples.
(4) The AFD method is further demonstrated for real-world composite applications through a complex frame, achieving ultralight weight and continuously aligned fibres along the curved sections.

In future works, the contribution of air void reduction to the improved mechanical performance and change of failure mode will be further investigated by incorporating progressive failure analysis in the developed image-based finite element models incorporating the fibre-matrix interface.

CRediT authorship contribution statement

Ka Zhang: Writing – original draft, Visualization, Validation, Software, Methodology, Formal analysis, Data curation. **Conchúr Ó Brádaigh:** Writing – review & editing, Supervision. **Dongmin Yang:** Writing – review & editing, Supervision, Resources, Project administration, Methodology, Funding acquisition, Conceptualization.

Declaration of competing interest

The authors declare that they have no known competing financial interests or personal relationships that could have appeared to influence the work reported in this paper.

Acknowledgement

The authors would like to acknowledge EPSRC CIMComp Hub (EP/P006701/1-RIS3718946) for financial support of this research project, and the School of Engineering at the University of Edinburgh for providing a PhD scholarship for Ka Zhang.

Appendix A. Supplementary data

Supplementary data to this article can be found online at https://doi.org/10.1016/j.compscitech.2025.111460.

Data availability

Data will be made available on request.

References

[1] S.M.F. Kabir, K. Mathur, A.-F.M. Seyam, A critical review on 3D printed continuous fiber-reinforced composites: history, mechanism, materials and properties, Compos. Struct. 232 (2020) 111476.
[2] P.K. Penumakala, J. Santo, A. Thomas, A critical review on the fused deposition modeling of thermoplastic polymer composites, Compos. B Eng. 201 (2020) 108336.
[3] N. Van De Werken, H. Tekinalp, P. Khanbolouki, S. Ozcan, A. Williams, M. Tehrani, Additively manufactured carbon fiber-reinforced composites: state of the art and perspective, Addit. Manuf. 31 (2020) 100962.
[4] R. Matsuzaki, M. Ueda, M. Namiki, T.K. Jeong, H. Asahara, K. Horiguchi, T. Nakamura, A. Todoroki, Y. Hirano, Three-dimensional printing of continuous-fiber composites by in-nozzle impregnation, Sci. Rep. 6 (2016) 23058.
[5] A.N. Dickson, J.N. Barry, K.A. McDonnell, D.P. Dowling, Fabrication of continuous carbon, glass and Kevlar fibre reinforced polymer composites using additive manufacturing, Addit. Manuf. 16 (2017) 146–152.
[6] P. Zhuo, S. Li, I.A. Ashcroft, A.I. Jones, Material extrusion additive manufacturing of continuous fibre reinforced polymer matrix composites: a review and outlook, Compos. B Eng. (2021) 109143.
[7] K. Zhang, W. Zhang, X. Ding, Multi-axis additive manufacturing process for continuous fibre reinforced composite parts, Proced. CIRP 85 (2019) 114–120.
[8] R. Matsuzaki, T. Nakamura, K. Sugiyama, M. Ueda, A. Todoroki, Y. Hirano, Y. Yamagata, Effects of set curvature and fiber bundle size on the printed radius of curvature by a continuous carbon fiber composite 3D printer, Addit. Manuf. 24 (2018) 93–102.
[9] H. Shiratori, A. Todoroki, M. Ueda, R. Matsuzaki, Y. Hirano, Compressive strength degradation of the curved sections of 3D-printed continuous carbon fiber composite, Compos. Appl. Sci. Manuf. 142 (2021) 106244.
[10] H. Shiratori, A. Todoroki, M. Ueda, R. Matsuzaki, Y. Hirano, Testing method for evaluating mechanical properties of 3D printed CFRP with curved fibers by four-point bending test of L-shaped specimen, Composites Part C: Open Access (2021) 100187.
[11] G. Clancy, D. Peeters, V. Oliveri, D. Jones, R.M. O'Higgins, P.M. Weaver, A study of the influence of processing parameters on steering of carbon Fibre/PEEK tapes using laser-assisted tape placement, Compos. B Eng. 163 (2019) 243–251.
[12] D. Lukaszewicz, C. Ward, K.D. Potter, The engineering aspects of automated prepreg layup: history, present and future, Compos. Pt. B-Eng. 43 (3) (2012) 997–1009.
[13] V.S. Papapetrou, C. Patel, A.Y. Tamijani, Stiffness-based optimization framework for the topology and fiber paths of continuous fiber composites, Compos. B Eng. 183 (2020) 107681.
[14] X. Chen, G. Fang, W.-H. Liao, C.C.L. Wang, Field-based toolpath generation for 3D printing continuous fibre reinforced thermoplastic composites, Addit. Manuf. (2021) 102470.
[15] H. Zhang, J. Chen, D. Yang, Fibre misalignment and breakage in 3D printing of continuous carbon fibre reinforced thermoplastic composites, Addit. Manuf. 38 (2021) 101775.
[16] L.G. Blok, M.L. Longana, H. Yu, B.K.S. Woods, An investigation into 3D printing of fibre reinforced thermoplastic composites, Addit. Manuf. 22 (2018) 176–186.
[17] Y. Hu, R.B. Ladani, M. Brandt, Y. Li, A.P. Mouritz, Carbon fibre damage during 3d printing of polymer matrix laminates using the fdm process, Mater. Des. (2021) 109679.
[18] K. Zhang, H. Zhang, J. Wu, J. Chen, D. Yang, Improved fibre placement in filament-based 3D printing of continuous carbon fibre reinforced thermoplastic composites, Compos. Appl. Sci. Manuf. 168 (2023).
[19] H. Shiratori, A. Todoroki, M. Ueda, R. Matsuzaki, Y. Hirano, Mechanism of folding a fiber bundle in the curved section of 3D printed carbon fiber reinforced plastics, Adv. Compos. Mater. 29 (3) (2020) 247–257.
[20] G. Struzziero, M. Barbezat, A.A. Skordos, Consolidation of continuous fibre reinforced composites in additive processes: a review, Addit. Manuf. 48 (2021) 102458.
[21] R. Blanc, C. Germain, J.P.D. costa, P. Baylou, M. Cataldi, Fiber orientation measurements in composite materials, Compos. Appl. Sci. Manuf. 37 (2) (2006) 197–206.
[22] S. Li, P. Cheng, S. Ahzi, Y. Peng, K. Wang, F. Chinesta, J.P.M. Correia, Advances in hybrid fibers reinforced polymer-based composites prepared by FDM: a review on mechanical properties and prospects, Compos. Commun. 40 (2023).
[23] 3D printing with continuous fiber: a landscape. https://www.compositesworld.com/articles/3d-printing-with-continuous-fiber-a-landscape, August 2025.
[24] F. Baumann, J. Scholz, J. Fleischer, Investigation of a new approach for additively manufactured continuous fiber-reinforced polymers, Proc. Cirp. 66 (2017) 323–328.
[25] M. Ueda, S. Kishimoto, M. Yamawaki, R. Matsuzaki, A. Todoroki, Y. Hirano, A. Le Duigou, 3D compaction printing of a continuous carbon fiber reinforced thermoplastic, Compos. Appl. Sci. Manuf. 137 (2020) 105985.
[26] G. Chabaud, M. Castro, C. Denoual, A. Le Duigou, Hygromechanical properties of 3D printed continuous carbon and glass fibre reinforced polyamide composite for outdoor structural applications, Addit. Manuf. 26 (2019) 94–105.
[27] S. Gomarasca, D.M.J. Peeters, B. Atli-Veltin, C. Dransfeld, Characterising microstructural organisation in unidirectional composites, Compos. Sci. Technol. 215 (2021) 109030.
[28] M.J. Emerson, K.M. Jespersen, A.B. Dahl, K. Conradsen, L.P. Mikkelsen, Individual fibre segmentation from 3D X-ray computed tomography for characterising the fibre orientation in unidirectional composite materials, Compos. Appl. Sci. Manuf. 97 (2017) 83–92.
[29] Y. Wang, M.J. Emerson, K. Conradsen, A.B. Dahl, V.A. Dahl, E. Maire, P.J. Withers, Evolution of fibre deflection leading to kink-band formation in unidirectional glass fibre/epoxy composite under axial compression, Compos. Sci. Technol. 213 (2021) 108929.
[30] M. Smith, ABAQUS/Standard User's Manual, 2009 version 6.9.
[31] H. Liu, D. Zeng, Y. Li, L. Jiang, Development of RVE-embedded solid elements model for predicting effective elastic constants of discontinuous fiber reinforced composites, Mech. Mater. 93 (2016) 109–123.
[32] Q. Liu, L. Gorbatikh, S.V. Lomov, A combined use of embedded and cohesive elements to model damage development in fibrous composites, Compos. Struct. 223 (2019).
[33] A. Avanzini, D. Battini, L. Giorleo, Finite element modelling of 3D printed continuous carbon fiber composites: embedded elements technique and experimental validation, Compos. Struct. 292 (2022).
[34] A. Şık, E. Gürses, B. Sabuncuoglu, Development of a procedure to model the mechanical behavior of composites with embedded element method by considering the matrix non-linearity, Compos. Struct. 259 (2021).

[35] Q. Liu, S.V. Lomov, L. Gorbatikh, The interplay between multiple toughening mechanisms in nanocomposites with spatially distributed and oriented carbon nanotubes as revealed by dual-scale simulations, Carbon 142 (2019) 141–149.
[36] B.N. Fedulov, F.K. Antonov, A.A. Safonov, A.E. Ushakov, S.V. Lomov, Influence of fibre misalignment and voids on composite laminate strength, J. Compos. Mater. 49 (23) (2014) 2887–2896.
[37] J. Hapke, F. Gehrig, N. Huber, K. Schulte, E.T. Lilleodden, Compressive failure of UD-CFRP containing void defects: in situ SEM microanalysis, Compos. Sci. Technol. 71 (9) (2011) 1242–1249.
[38] Q. He, H. Wang, K. Fu, L. Ye, 3D printed continuous CF/PA6 composites: effect of microscopic voids on mechanical performance, Compos. Sci. Technol. 191 (2020) 108077.
[39] W.V. Liebig, C. Viets, K. Schulte, B. Fiedler, Influence of voids on the compressive failure behaviour of fibre-reinforced composites, Compos. Sci. Technol. 117 (2015) 225–233.
[40] J. Chen, L. Wan, K. Nelms, G. Allegri, D. Yang, Failure analysis of unidirectional CFRP composites with the coupled effects of initial fibre waviness and voids under longitudinal compression, Compos. Struct. 347 (2024).
[41] J.S. Mayes, A.C. Hansen, Composite laminate failure analysis using multicontinuum theory, Compos. Sci. Technol. 64 (3–4) (2004) 379–394.
[42] Standard Test Method for Measuring the Curved Beam Strength of a Fiber-Reinforced Polymer-Matrix Composite.
[43] A.S.f. Testing, Materials, Standard Test Method for Measuring the Curved Beam Strength of a fiber-reinforced polymer-matrix Composite, ASTM International, 2012.
[44] R. Gutkin, S.T. Pinho, P. Robinson, P.T. Curtis, A finite fracture mechanics formulation to predict fibre kinking and splitting in CFRP under combined longitudinal compression and in-plane shear, Mech. Mater. 43 (11) (2011) 730–739.